Local electrical characterization of cadmium telluride solar cells using low-energy electron beam

Heayoung P. Yoon[1, 3], Paul M. Haney[1], Dmitry Ruzmetov[1, 3], Hua Xu[1, 3], Marina S. Leite[1, 3], Behrang H. Hamadani[2], A. Alec Talin[1], Nikolai B. Zhitenev[1]

[1]*Center for Nanoscale Science and Technology, National Institute of Standards and Technology, Gaithersburg, MD 20899, USA*

[2]*Energy and Environment Division, National Institute of Standards and Technology, Gaithersburg, Maryland, 20899, USA*

[3]*Maryland Nanocenter, University of Maryland, College Park, MD 20742, USA*

We investigate local electronic properties of cadmium telluride solar cells using electron beam induced current (EBIC) measurements with patterned contacts. EBIC measurements are performed with a spatial resolution as high as ≈20 nm both on the top surface and throughout the cross-section of the device, revealing a remarkable degree of electrical inhomogeneity near the *p-n* junction and enhanced carrier collection in the vicinity of grain boundaries (GB). Simulation results of low energy EBIC suggest that the band bending near a GB is downward, with a magnitude of at least 0.2 eV for the most effective current-collecting GBs. Furthermore, we demonstrate a new approach to investigate local open-circuit voltage by applying an external bias across electrical contact with a point electron-beam injection. The length scale of the nanocontacts is on the length scale of a single or a few grains, confining current path with highly localized photo-generated carriers.

1. Introduction

Chalcogenide and chalcopyrite photovoltaic (PV) materials are attractive options for thin film solar cells due to their effective optical absorption and inexpensive fabrication processes [1] [2]. Among these thin film PVs, cadmium telluride (CdTe) solar cells represent one of the most successful solar energy technologies on the market today. However, at ≈13 % efficiency, commercial module performance is still well below the theoretical maximum value (≈28 % under 1 sun) [2]. The underlying physical mechanisms for the discrepancy between the actual and theoretical efficiencies are presently not well understood. Grain boundaries, for example, are known to have a high concentration of defects and impurities which generally increase carrier recombination and thus adversely affect cell performance. In contrast, it has been suggested that compositional non-uniformity and/or surface states present at grain boundaries in the CdTe absorber induce a space-charge region, which can be beneficial for minority carrier collection [3, 4]. The effect of grain boundaries on the open-circuit voltage (V_{oc}) is another important consideration, as V_{oc} for these materials is still well below its theoretical maximum [5,6]. Therefore, the details of how microstructure affects macroscopic performance must be addressed in order to optimize performance of PV materials comprised of a high density of grains.

Characterization techniques based on scanning probe and focused electron beams are increasingly used for investigating microstructures, compositions, and optoelectrical properties of thin film solar cells [7,8]. Electron beam induced current (EBIC) is one such method, and is frequently used to map hot carrier recombination in semiconductors by rastering an electron beam in a scanning electron microscope (SEM) while selectively collecting minority carriers using a Schottky or a *p-n* junction [9]. The EBIC contrast reflects the local efficiency of carrier collection, which is determined by local built-in and applied electric fields, as well as the carrier

2

recombination rate. To improve the signal-to-noise ratio and decrease the effects of surface recombination, high energy beams (>10 keV) are typically used for EBIC measurements [10].

In this work, we extend traditional EBIC measurements on photovoltaic devices in three ways: (1) use of low energy beams (<5 keV) in order to map the photocurrent response with a spatial resolution adequate to probe the material inhomogeneity, (2) use of a patterned contact on the CdTe layer to confine the current path, and (3) application of external bias across the electrical contacts, which enables the measurement of current-voltage (*I-V*) characteristics for these confined current paths with highly localized photo-generated carriers. Using these techniques, we find substantial inhomogeneity in material properties within the *p-n* junction, and a band bending exceeding 0.2 eV near GBs which most effectively facilitate charge collection. The paper is organized as follows: in Sections 2 and 3 we describe experimental and modeling details, respectively. In Section 4, we first present low energy cross-sectional EBIC data, followed by top-down EBIC data with a patterned top contact. We then discuss simulation results, showing that the low energy EBIC signal is sensitive to the magnitude of the local electric field, and the top-down EBIC signal line-shape can be used to estimate the band bending near a grain boundary. Finally, we present *I-V* data obtained with a nanocontact.

2. Experimental

All measurements in this work were performed on thin film solar cell fragments extracted from a commercial solar module, consisting of *p*-type CdTe (≈3.5 μm) / *n*-type cadmium sulfide (CdS; ≈50 nm) sandwiched between two glass substrates (≈3 mm). The large module was cut into small pieces (< 3 cm × 3 cm), and the polymeric layer (ethylene vinyl acetate) was slowly peeled off a tempered glass, exposing a stack of *p*-CdTe / *n*-CdS / transparent conductive oxide

(TCO) films on top of the other glass substrate. To make Ohmic contact to the *p*-CdTe, we either used the native metallization remaining on the surface after the extraction process or deposited platinum (Pt) contacts using a focused ion beam (FIB) with a size down to ≈0.5 μm × 0.5 μm. The second common contact to the TCO layer was made using indium solder. Electrical measurements are performed in a SEM equipped with a nano-manipulator used for placement of a tungsten probe (100 nm tip radius) on top of the contacts to *p*-CdTe. *I-V* data were collected using an external source-measuring unit, while EBIC images were obtained using a low-noise current amplifier under computer control.

3. Model details

To assist in interpreting the experimental results, we perform 2D finite element simulations. The model consists of coupled drift-diffusion and Poisson equations, with Shockley-Read-Hall recombination. The generation bulb is a Gaussian, with length scale set by the beam energy according to: $R = 0.043 \times \left(E_{beam} / \rho \right) \left[\text{g cm}^{-3} \text{ keV } \mu\text{m} \right]$, where ρ is the material density. The distance between the top surface and the excitation peak is $0.3R$, while the width of the excitation is $\sigma = R / \sqrt{15}$ [23].

We consider two geometries: the first is a simple *p-n* junction with large contacts, which we use to study the low energy cross-sectional EBIC signal (see Fig. 3a). The second geometry has a localized contact on the *p*-type region, a back contact on the entire length of the *n*-type region, and a grain boundary (see Fig. 4b). We model the grain boundary (GB) by imposing a fixed electrostatic potential difference ΔE between the neutral *p*-region and the GB center [21]. We vary the band bending ΔE, and the recombination velocity at the GB center S_{GB}. The model parameters are given in Table 1. The values of top surface and hole contact recombination

velocity were obtained by fitting high energy EBIC data (> 10 keV) to analytic models, as in Ref. [24].

Table 1. Model parameters

Parameter	CdS	CdTe
Layer thickness [µm]	0.12	3.6
Band gap [eV]	2	1.5
Conduction band offset [eV]	0	-0.1
Doping density [cm^{-3}]	10^{17}	10^{15}
Hole mobility [$cm^2\ V^{-1}\ s^{-1}$]	320	320
Electron mobility [$cm^2\ V^{-1}\ s^{-1}$]	40	40
Minority carrier lifetime [ns]	0.8	0.8
Majority (minority) carrier recombination velocity at contact [cm/s]	$10^8\left(10^8\right)$	$10^8\left(3\times10^4\right)$
Generation rate [$cm^{-3}\ s^{-1}$]	n/a	6×10^{24}
Top surface recombination velocity [cm/s]	1.8×10^6	1.8×10^6

4. Results and discussion

The baseline PV performance of the extracted CdTe specimens evaluated under 1000 W/m^2 (1 sun) is ≈12 % efficiency, with a J_{sc} of 23.3 mA/cm^2, a V_{oc} of 820 mV, and fill factor of 64 %, indicating that device properties are mainly preserved after the extraction processes. Fig. 1(a) shows an SEM image of the cell. The grain size varies from ≈0.1 µm to ≈2 µm with a peak-to-peak surface roughness of ≤0.5 µm, indicating highly inhomogeneous microstructure, typical of a polycrystalline CdTe absorber. A simultaneously collected EBIC image at 5 kV is shown in Fig. 1(b). The current is collected with a probe tip positioned on an isolated flake of the native metallization (contact area ≈5 µm × 10 µm). The bright contrast seen at many grain boundaries (GBs) indicates higher minority carrier collection for excitations at grain boundaries than at grain

interiors (GIs), consistent with prior work [11]. A line scan corresponding to the EBIC signal collected for two adjacent grains is plotted in Fig. 1(c), where the current peaks (≈6 nA) at each GB and reaches a minimum (≈1 nA) at the center of the GI. As we discuss later, we use the magnitude of signal enhancement at the GB (a factor of 5 to 6) in order to estimate the band bending at these GB. The decay length of the EBIC signal is characteristic of (at least) two length scales: the space-charge depletion width and the minority carrier diffusion length. Some grain boundaries show a plateau (<200 nm) at the peak of the EBIC current, which we attribute to the depletion width (Fig.1c, ①). The decay of the peak EBIC signal from the GB toward the GI can be fit with a simple exponential $I_{EBIC} \approx \exp(-x/L_c)$, where L_c is an effective minority carrier diffusion length. The extracted value of L_c from the EBIC line scan is in a range of ≈100 nm to ≈800 nm.

To characterize the local response throughout the entire *p-n* junction region, we use a FIB to cut a cross-section through the device. The FIB process additionally results in a smoother surface compared to the native top surface, minimizing the effect of surface roughness [14]. Simultaneously obtained SEM and EBIC images on the cross-sectioned device are shown in Figs 2(a) and 2(b), respectively. The magnitude and line shape of the EBIC signal near the *p-n* junction can be similar to that near some grain boundaries. However, the plateau width and decay length in the signal at different grain boundaries or at different positions along the *p-n* junction vary significantly throughout the sample.

To assist in interpreting these data, we perform two sets of simulations: the first simulation geometry is shown in Fig. 3(a), and is intended to clarify the cross-sectional EBIC data taken at low energies. At low energies, the length scale of the excitation bulb is smaller than that of the material inhomogeneity. Analytic EBIC models are derived for homogeneous

materials [12], so that their application to strongly inhomogeneous materials like CdTe is not straightforward. Fig. 4 shows the simulated signals for a range of beam energies, along with the signal predicted by the commonly used EBIC models of Refs [22, 25]. For high beam energies, the analytical model agrees well with the simulation results. However, for low beam energies there are deviations between the analytic expression and the simulation, especially near the edge of depletion region. The source of this discrepancy is the approximation made in the analytic treatments that all carriers within the depletion region are collected. In fact, the collection probability for carriers within the depletion region is less than 1 due to the high surface recombination. In general, the signal is substantially decreased; however the signal line-shape not adequately captured by the analytical model may offer an additional route to probing material properties.

To study how the low-energy EBIC signal depends on the electric field in the depletion region, we vary the band bending in a single CdTe layer for a fixed low-energy beam [20]. The results are shown in the inset of Fig 4. For small band bending (or small electric field), the maximum signal is reduced, as the charge separation from the weak electric field is not sufficient to overcome the strong surface recombination. We argue on the basis of Fig. 4 that the low-energy EBIC signal is a very sensitive probe of the *magnitude* of local electric fields (for sufficiently small fields, so that the collection probability is less than 1 in the field region). The quantitative features of the inset of Fig. 4 are not universal however, and depend on parameters such as S_{vac} and L_D. Therefore some *a priori* knowledge of these parameters is required for quantitative estimates of electrostatic fields. Here, as mentioned above, we determine these parameters from the high-energy EBIC that effectively averages the data over multiple grains.

The interpretation of low energy EBIC signals in terms of local electric fields leads to the surprising conclusion that the electric field at the *p-n* junction and at the GBs is highly inhomogeneous. This is seen in Fig. 2(b), which shows significant variation of the EBIC signal even deep within the nominal depletion region. This may be due to a variety of factors, including inhomogeneous doping of grains, which would lead to variations in band bending and diffusion lengths between grains. Another possibility is the presence of localized states at the vacuum surface whose density and energetic position depend on the crystallographic orientation of the grain. These states could lead to a band bending at the vacuum surface, changing the effective surface recombination velocity in different grains. Finally sulfur diffusion and inhomogeneous CdTe coverage could lead to an inhomogeneous electric field at the junction interface. We believe that the signal line-shape is indicative of real material structure, and that it may be ascertained with more systematic studies in the future, in conjunction with modeling efforts.

We next simulate the top-down EBIC experiment, with the geometry shown in Fig. 3(b). We model the GB by imposing a fixed electrostatic potential difference ΔE between the neutral *p*-region and the GB center [21]. The two parameters we vary are the band bending ΔE and the recombination velocity at the GB center S_{GB}. As shown in previous works, downward band bending at a grain boundary facilitates charge collection, while for some cases, increased recombination at the GB can reduce charge collection [17]. Fig. 3(c) shows the overall current distribution (minority and majority currents) for an excitation away from the contact. The electron (minority carriers) current flows to the GB and to the CdS layer. The hole current flows downward from the excitation point to the junction, then around the GB, and finally back upward to the hole-collecting contact.

Fig. 5(a) shows the simulated EBIC signals for $S_{GB} = 0$ (no extra recombination at the GB center) and a range of band bending ΔE for the beam energy of 5 keV. As the excitation is positioned near the GB, we find increased current only for sufficiency large ΔE. This is because the downward band bending generally increases bulk recombination, due to the associated higher minority carrier density near the GB. To compensate for this region of increased recombination, the charge-separating field must be sufficiency large so that the total *net* recombination is reduced. To make a connection with experimental data, we take the "signal enhancement" as the key metric − the ratio of the maximum current at a GB to the current within a grain interior. Experimentally this value is between 5 and 6 for the GB in Fig. 1(b). There is a distribution of this value over all GB and this particular ratio is on the high side of the distribution. For $S_{GB} = 0$, we find a factor of 6 enhancement in charge collection requires a band bending of 0.21eV (see inset of Fig. 5a).

In Fig. 5(b), we show the signal enhancement as a function of both the band bending and GB recombination velocity. As the GB recombination velocity increases, the required band bending for signal enhancement also increases. This is again due to the need for a larger field and more charge separation to compensate for increased recombination. There is a set of values of ΔE and S_{GB} that result in simulated EBIC signals that are consistent with the experiment − shown in the dashed white line of Fig. 5(b). We cannot ascertain which parameter set of $\left(\Delta E, S_{GB} \right)$ is the most appropriate for our sample. However, the required band bending for signal enhancement is an increasing function of S_{GB}. We can therefore put a lower bound on ΔE, as shown in Fig. 5, and we find that ΔE must exceed 0.2 eV. We note that the similar estimate of the band bending at GBs (although less constrained due local inhomogeneity) can be obtained from the cross-sectional data comparing EBIC profiles at *p-n* junction and GBs. We therefore

9

conclude that the use of this technique can offer an informative way to probe the properties of grain boundaries, and a lower bound to the band bending near the GB of 0.2 eV can be assigned.

We finally turn to the application of an external bias in the EBIC experimental geometry, which would provide key insights into the role of grain boundaries in the overall device efficiency. The grain boundaries as current collectors enhance J_{sc}, but at the same time as recombination centers can reduce the V_{oc} due to the increase in dark recombination current[1].. Given that the detrimental impact of grain boundaries may be mostly manifest at a nonzero applied voltage, it seems critical to probe their properties in this regime. Six injection spots corresponding to grain boundaries (GBs) and grain interiors (GIs) are selected in three different regions across the p-CdTe absorber, as shown in Fig. 2(c). In all cases, the n-CdS is grounded and voltage is applied to the metal contact to p-CdTe. A higher short-circuit current ($V_{app} = 0$) is measured when the beam is injected in the vicinity of the GB as compared to the GI for each region investigated, further illustrating that GBs act as channels for current flow rather than minority carrier recombination sinks. We also find that the voltage at zero current V_{oc}) increases as local I_{sc} increases regardless of the specific location (*i.e.*, GB *vs.* GI).

For this geometry, the length scale of the contacts is two to four times larger than the absorber thickness, so that V_{oc} is a non-local property which cannot be ascribed to a specific grain boundary. This is because in the simplest approximation V_{oc} can be associated with the voltage at which the dark current in forward bias cancels the EBIC current. The value of this dark current depends on the material properties of the *entire* region (as well as the various contact interfaces) through which current flows, which will include many grain boundaries, and regions of grain interior. To introduce the notion of a *local V_{oc}*, we experimentally restrict the

---

[1] $V_{oc} = V_T \ \ln(I_{sc}/I_0)$. V_{oc} is open-circuit voltage, V_T is thermal voltage, I_{sc} is short-circuit current, and I_0 is dark current.

volume through which the injected current flows. This is accomplished with a contact on the p-type layer surface with a size smaller than the absorber thickness.

To realize this geometry experimentally, we fabricate a 500 nm-thick Pt contact ($\approx$1 μm × 1 μm) on top of a single grain on p-CdTe using electron beam induced deposition in a FIB system. I-Vs collected under local carrier excitation at 3 kV at GBs and GIs near the nano-probe are shown in Fig. 6, along with an EBIC image displaying similar contrast to that shown in Fig 1. As observed in the cross-sectional local I-Vs, the local V_{oc} increases as local I_{sc} increases: we find local $V_{oc} \approx$0.15 V and $\approx$0.25 V at GIs and GBs, respectively. These low values of local V_{oc} are mainly due to the reduced local I_{sc} obtained with the nanocontact as compared to the large-area contact in a full PV operation

Modeling a point-contact geometry demonstrates that most of the injected current is confined to a region below the contact, and that the current spreading scales as the layer thickness. However, even if the contact is positioned away from a GB, the nearest grain boundary carries a large portion of the dark current (see Fig. 3(d)) introducing an effective non-locality into the measurements even in the case of the nanocontact geometry. The simulation also illustrate that the GBs are a major pathway for the overall leakage current. However, the present measurement set is not yet sufficiently constrained to accurately quantify the impact of the GBs on the V_{oc}.
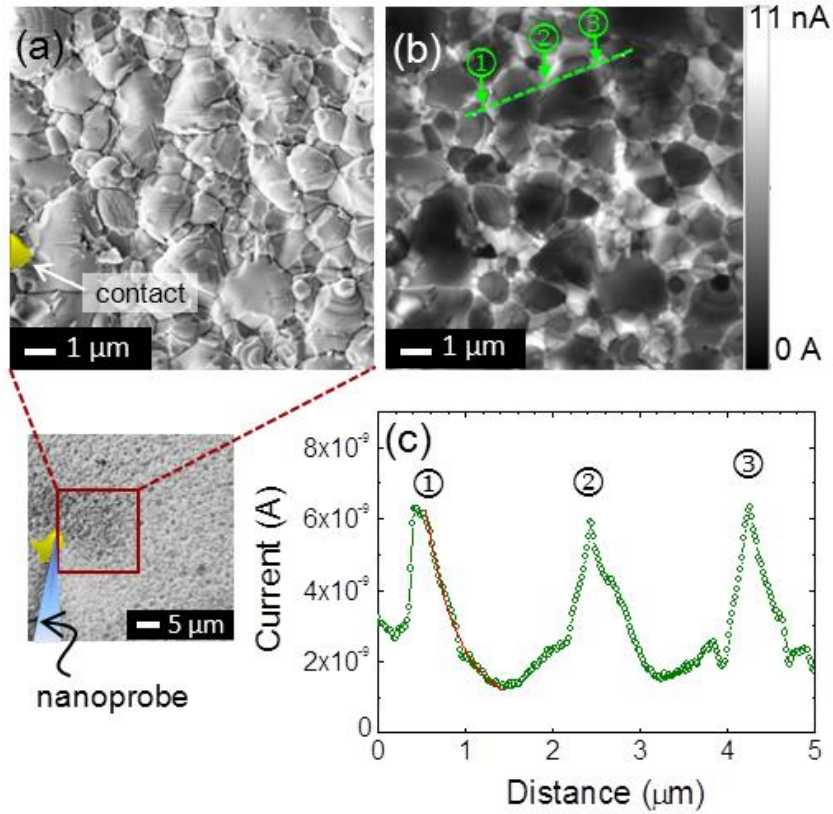

5. Conclusions

In summary, we use low energy EBIC to probe carrier recombination in a polycrystalline p-CdTe / n-CdS solar cell with the spatial resolution required to assess the material inhomogeneity. Plan-view and cross-sectional EBIC images show that a large fraction of grain

boundaries display higher current collection as compared to grain interiors. We measure local I-Vs using nanocontacts, which demonstrates that the local V_{oc} approximately tracks with the local I_{sc} for excitation both at the grain boundary and at the grain interior. Further studies to elucidate the specific structure and chemical composition of the grain boundaries as 3D minority carrier collectors would provide essential information to enhance PV performance in CdTe based solar cells.

Figures

Fig. 1. (a) SEM image of a CdTe / CdS solar cell where a tungsten probe tip is placed on a native metal contact (≈5 μm × 10 μm). (b) Corresponding EBIC image with an acceleration voltage of 5 kV and a beam current (I_b) of 300 pA. We estimate the generation volume to be ≈(115 nm)^3 at this excitation condition [9]. (c) EBIC linescan across adjacent two grains, showing a peak current (≈6 nA) at GBs and a valley current (≈1 nA) at the center of GIs, respectively[2]. Extrapolated characteristic lengths (L_c) are in a range of ≈100 nm to ≈800 nm. A representative curve fit (red solid line) shows L_c of 374 nm ± 19 nm.

---

[2] The EBIC current corresponds with the negative current produced by the minority carrier (electrons). The polarity of the EBIC current was inverted in this image for convenience.

13

Fig. 2. Cross-sectional (a) SEM and (b) 5 kV EBIC images, showing bright current contrast in the vicinity of *p-n* junction and the GBs. (c) *I-V* curves under local carrier generation at GIs (1, 3, 5) and GBs (2, 4, 6). In all cases *n*-CdS was grounded and voltage was applied to the metal contact of *p*-CdTe. Uncertainty due to the electrical background noise signal is ≈200 pA (one standard deviation).
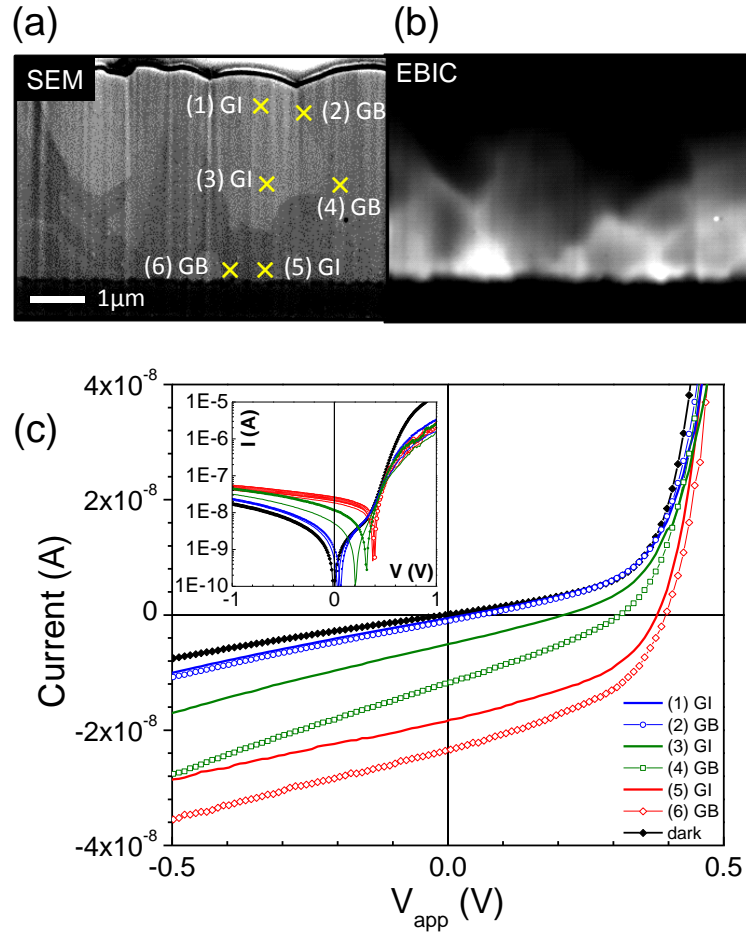
Fig. 3. (a) Geometry for the cross-sectional EBIC simulation. The black arrow shows the position of EBIC excitation, which is scanned in the simulation. The color indicates equilibrium electrostatic potential. (b) Geometry for the top-down EBIC simulation. The GB band bending is 0.26 eV for this case, and color is again the equilibrium electrostatic potential. (c) EBIC spatial distribution in the top-down case at zero applied voltage. The black arrow indicates the excitation point. (d) The forward dark current at V_{oc}. A large portion of the current is carried by the center of the GB.

Fig. 4. Simulated and analytical models of spatial dependence of EBIC signal for *n*-CdS / *p*-CdTe heterojunction, for different beam energies. For low energies, there is a discrepancy near the edge of depletion region, which is located at 1.1 μm. The inset shows simulated internal quantum efficiency corresponding to a maximum of EBIC signal for hypothetical *p-n* junction, as a function of band bending ΔE, for fixed beam energy of 5 keV. The analytic curve shown is calculated from the convolution of the generation profile with Eq. (20) of Ref. [25], which for these parameters is nearly identical to the more complicated Eq. (A14) of Ref. [22].

Fig. 5 (a) Simulated EBIC signal in top-down geometry for a GB with no extra recombination, for a set of ΔE values. The inset shows the "signal enhancement": the internal quantum efficiency (IQE) at the GB, normalized by its value at a remote grain interior, for $\Delta E = 0.21$. There is an enhancement at the GB of a factor of ≈ 6, consistent with experimental results (b) The signal enhancement for a range of ΔE and S_{GB}. The white dashed line shows the region of GB parameter space for which there is signal enhancement of 6.
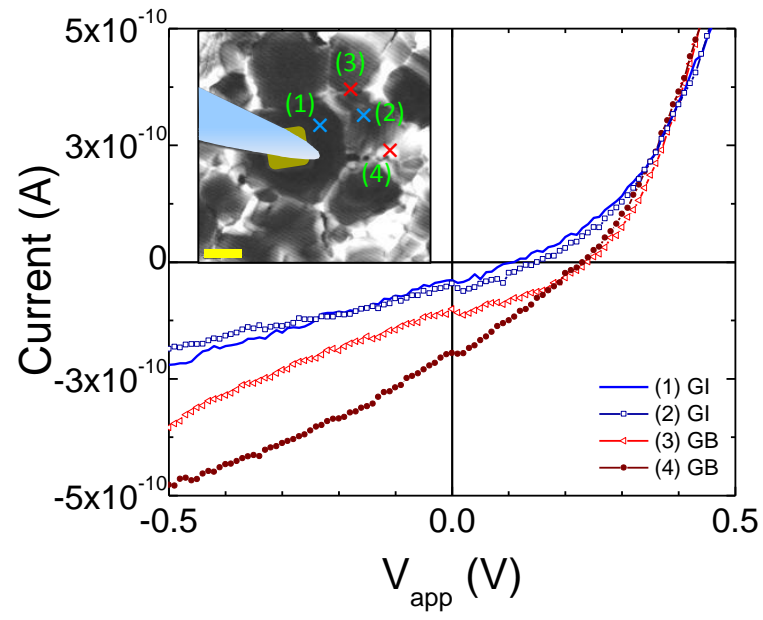
Fig. 6. Local *I-V* characteristics with a nanocontact under a local carrier generation at GIs (1, 2) and GBs (3, 4). The inset shows an EBIC image of the device (3 kV, I_b = 270 pA; scale bar: 1 μm)

Acknowledgement

References

[1] C.A. Wolden, J. Kurtin, J.B. Baxter, I. Repins, S.E. Shaheen, J.T. Torvik, A.A. Rockett, V.M. Fthenakis, E.S. Aydil, Photovoltaic manufacturing: Present status, future prospects, and research needs, J Vac Sci Technol A, 29 (2011).

[2] P.K. Nayak, J. Bisquert, D. Cahen, Assessing Possibilities and Limits for Solar Cells, Adv Mater, 23 (2011) 2870-2876.

[3] I. Visoly-Fisher, S.R. Cohen, K. Gartsman, A. Ruzin, D. Cahen, Understanding the beneficial role of grain boundaries in polycrystalline solar cells from single-grain-boundary scanning probe microscopy, Adv Funct Mater, 16 (2006) 649-660.

[4] W. Jaegermann, A. Klein, T. Mayer, Interface Engineering of Inorganic Thin-Film Solar Cells - Materials-Science Challenges for Advanced Physical Concepts, Adv Mater, 21 (2009) 4196-4206.

[5] J.R. Sites, J.E. Granata, J.F. Hiltner, Losses due to polycrystallinity in thin-film solar cells, Sol Energ Mat Sol C, 55 (1998) 43-50.

[6] S. Siebentritt, What limits the efficiency of chalcopyrite solar cells?, Sol Energ Mat Sol C, 95 (2011) 1471-1476.

[7] D. Abou-Ras, R. Caballero, C.H. Fischer, C.A. Kaufmann, I. Lauermann, R. Mainz, H. Monig, A. Schopke, C. Stephan, C. Streeck, S. Schorr, A. Eicke, M. Dobeli, B. Gade, J. Hinrichs, T. Nunney, H. Dijkstra, V. Hoffmann, D. Klemm, V. Efimova, A. Bergmaier, G. Dollinger, T. Wirth, W. Unger, A.A. Rockett, A. Perez-Rodriguez, J. Alvarez-Garcia, V. Izquierdo-Roca, T. Schmid, P.P. Choi, M. Muller, F. Bertram, J. Christen, H. Khatri, R.W. Collins, S. Marsillac, I. Kotschau, Comprehensive Comparison of Various Techniques for the Analysis of Elemental Distributions in Thin Films, Microsc Microanal, 17 (2011) 728-751.

[8] M.J. Romero, M.M. Al-Jassim, R.G. Dhere, F.S. Hasoon, M.A. Contreras, T.A. Gessert, H.R. Moutinho, Beam injection methods for characterizing thin-film solar cells, Prog Photovoltaics, 10 (2002) 445-455.

[9] H.J. Leamy, Charge Collection Scanning Electron-Microscopy, J Appl Phys, 53 (1982) R51-R80.

[10] J.I. Hanoka, R.O. Bell, Electron-Beam-Induced Currents in Semiconductors, Annu Rev Mater Sci, 11 (1981) 353-380.

[11] P.R. Edwards, S.A. Galloway, K. Durose, EBIC and luminescence mapping of CdTe/CdS solar cells (vol 361, pg 364, 2000), Thin Solid Films, 372 (2000) 284-291.

[12] C. Donolato, Evaluation of Diffusion Lengths and Surface Recombination Velocities from Electron-Beam Induced Current Scans, Appl Phys Lett, 43 (1983) 120-122.

[14] H.P. Yoon, D. Ruzmetov, P.M. Haney, M.S. Leite, B.H. Hamadani, A.A. Talin, N.B. Zhitenev, High-Resolution Local-Current Measurement of CdTe Solar Cells, Conference Record of the Thirty-Eighth IEEE Photovoltaic Specialists Conference - 2012, (2012).

[17] W. K. Metzger, M. Gloeckler, The Impact of Charged Grain Boundaries on Thin-Film Solar Cells and Characterization, J Appl Phys 98 (2005), 063701.

[18] J. Rechid, A. Kampmann, R. Reineke-Koch, Thin Solid Films, 21 (2000) 198-202.

[19] J. Oualid, C.M. Singal, J. Dugas, J.P. Crest, H. Amzil, Influence of Illumination on the Grain-Boundary Recombination Velocity in Silicon, J Appl Phys, 55 (1984) 1195-1205.

[20] To easily control the band bending, we take a hypothetical system consisting of a single CdTe layer, with the following boundary conditions at the p-type contact: $p_1 = N_A$, $n_1 = N_c N_v \exp\left(-E_g / kT\right)/p_1$, $V = 0$, and the following boundary conditions at the other contact: $p_1 = N_A \exp\left(-\Delta V / kT\right)$, $n_1 = N_c N_v \exp\left(-E_g / kT\right)/p_1$, $V = -\Delta V$. Here N_A is the bulk acceptor density, and $N_{c(v)}$ is the conduction (valence) effective density of states. We found that the details of the relatively very small *n*-type layer do not affect the results of the CdTe-CdS *p-n* junction, so that a system with only *p*-type material as described here will suffice here.

[21] Our treatment of the charge near the GB is simplified relative to other commonly used models, such as that found in Ref. [17]. We intentionally chose this approach because in more realistic models, the band bending near a GB will itself depend on the illumination position and magnitude. To remove this extra convolution in the data, we keep the band bending ΔE fixed, and calculate the response for a range of fixed ΔE. For CdTe, illumination will generally increase the occupancy of the GB states, thereby reducing the band bending. This implies that the equilibrium band bending will be greater than the parameters given in this work.

[22] O. Von Roos and K. L. Luke, Analysis of the Interaction of an Electron Beam With Back Surface Field Solar Cells, J. Appl. Phys., 54 (1983) 3938-3942.

[23] H. J. Fitting, H. Glaefeke, and W. Wild, Electron Penetration and Energy Transfer in Solid Targets, Phys. Stat. Sol. (a), 32 (1977) 185-190.

[24] R. Kniese, M. Powalla, and U. Rau, Evaluation of Electron Beam Induced Current Profiles of Cu(In,Ga)Se2 Solar Cells With Different Ga-contents, Thin Solid Films, 517 (2009), 2357-2359.

[25] C. Donolato, On the Analysis of Diffusion Length Measurements By SEM, Solid State Electronics, 25 (1982) 1077-1081.